

*Article*

## A Two-Dimensional Numerical Investigation of Aerodynamic Noise from an Inclined Plate

Nonwarit Borvornsareepirom<sup>a</sup> and Watchapon Rojanaratanangkule<sup>b,\*</sup>

Department of Mechanical Engineering, Faculty of Engineering, Chiang Mai University,  
Chiang Mai 50200, Thailand

E-mail: <sup>a</sup>nonwarit@outlook.com, <sup>b\*</sup>watchapon.roj@eng.cmu.ac.th (Corresponding author)

**Abstract.** Direct computations of acoustic noise of flow over an inclined plate are performed at two Mach numbers by solving the compressible Navier–Stokes equations without invoking any form of modelling. The flat plate has a sharp leading edge and sharp trailing edge and is inclined at incidence of 20°. The simulations are performed at a chord-based Reynolds number of 1000, and the freestream Mach numbers of 0.4 and 0.6. The numerical results reveal the effect of the Mach number on both of the hydrodynamic near-field and the acoustic far-field. Increasing the Mach number results in an increase in the shedding frequency and a decrease in the acoustic wavelength. The directivity plots show that additional lobes are present on the plate suction side at higher Mach number.

**Keywords:** Far-field noise, compressible flow simulation, inclined plate, vortex dynamics, boundary data immersion method.

ENGINEERING JOURNAL Volume 26 Issue 6

Received 21 November 2021

Accepted 5 June 2022

Published 30 June 2022

Online at <https://engj.org/>

DOI:10.4186/ej.2022.26.6.41

## 1. Introduction

In the area of aeroacoustics, noise is generated predominantly by the interaction between pressure fluctuations with a solid surface. The pressure fluctuations are caused by various reasons, e.g. turbulent boundary layer flows, incident gusts, or an unsteady wake. Once the noise is generated, it can radiate over a long distance and may be hazardous if its sound level is higher than a certain value. Therefore, it is necessary to meet noise regulations to avoid adverse effects.

Acoustic sounds radiated by flow over a bluff body, especially an airfoil, have been investigated by several researchers due to its vast range of applications in aeronautical engineering including aero-engines, wind turbines, high-lift devices, etc. The airfoil self-noise has their main sources listed as follows: (I) a weak source from the leading-edge (LE) separation bubble; (II) the traditional noise from the pressure fluctuations contacted with the trailing-edge (TE); (III) an extra noise generated from the vortex near the wake zone [1]. From previous research, it is found that the strongest source of airfoil self-noise is caused by the trailing edge. The intensity of sound generated from the TE noise is proportional to  $M^5$  [2] (where  $M$  is the Mach number), while that radiated in free space can be approximated as  $M^6$  [3, 4]. Therefore, the TE noise is one of the main sources of aircraft noise for subsonic flow.

The theories of TE noise prediction can be categorised into three types [5]: (I) theories based on Lighthill's acoustic analogy [3, 4], developed by, e.g., Ffowcs Williams and Halls [2]; (II) theories based on the solution of special problems approximated by the linearised hydro acoustic equations, such as that of Amiet [6]; and (III) ad hoc models that determine the strength and the multipole types of the source distributions via the use of empirical methods. Howe [5] concluded that the results from all the three analogies above are similar at small Mach numbers. This conclusion was confirmed by the TE noise experiments of a NACA0012 airfoil of Brooks and Hodgson [7]. From previous predictive research, the use of Amiet's trailing-edge noise theory is the most popular method to predict the far-field noise since only the surface pressure difference on the upstream of the trailing-edge is required, rather than having to specify the full detail of the noise sources. Sandberg *et al.* [8] compared the results between the sound pressure computed directly via the use of direct numerical simulation (DNS) and the Amiet's trailing-edge noise theory. It was found that the high amplitude downstream pointing lobes of the sound pressure observed in DNS are accurately predicted by the Amiet's trailing-edge noise theory. Previous experimental [9, 10] and numerical studies using hybrid approaches [11], that com-

bine aeroacoustic integral methods with a suitable CFD technique to predict far-field sound radiation, and direct computations (such as DNS [12, 13, 14] and LES [15, 16]) on sound noise generated by an airfoil also shows that the airfoil trailing edge is a significant source of the tonal noise.

At relatively high incidence, flow over an airfoil usually consists of flow separation and vortex shedding. In order to investigate the vortex shedding mechanism and to avoid the effect of surface curvature, an inclined plate has frequently been employed [17, 18, 19]. The wake of an inclined plate consists of the vortices generated by the leading edge and the trailing edge. The strength of the leading-edge vortex (LEV) and trailing-edge vortex (TEV) was found to be unequal [17]. Additionally, the critical Reynolds number where three-dimensional instabilities occurs were found to depend on the angle of incidence [18]. The generation mechanism of the periodically unsteady aerodynamic forces of an inclined flat plate was investigated numerically [19]. It was found that the magnitude of the lift and drag depends on the vortex shedding processes. The plate exhibits the minimum lift when the LEV is moved furthest from the plate, while the TEV is still attached to the plate. On the other hand, the lift reaches its maximum value when the LEV grows to maturity near the trailing edge and initiates the shedding of the TEV.

Although flow over an inclined plate has been investigated tremendously, almost all of the studies were conducted in incompressible flow (e.g. particle image velocimetry measurement of Lam and Leung [20], LES [21] and DNS [17]). Therefore, the knowledge of acoustic waves is still missing. In this work, we will investigate the acoustic far-field generated by a laminar flow past an inclined plate by solving the compressible Navier–Stokes equations without any aeroacoustic models. The main aim is to use a high-fidelity numerical simulation to explore how the vortex shedding generated by a sharp inclined plate interacts with the sound noise.

## 2. Numerical Approach

The non-dimensional form of the conservation equations governing compressible flow written in a Cartesian coordinate system  $x_i$  can be expressed as

$$\frac{\partial \rho}{\partial t} + \frac{\partial}{\partial x_k}(\rho u_k) = 0, \quad (1)$$

$$\frac{\partial}{\partial t}(\rho u_i) + \frac{\partial}{\partial x_k}(\rho u_i u_k) = -\frac{\partial p}{\partial x_i} + \frac{\partial \tau_{ik}}{\partial x_k}, \quad (2)$$

$$\frac{\partial}{\partial t}(\rho E) + \frac{\partial}{\partial x_k}(\rho u_k E) = \frac{\partial}{\partial x_k}[u_i \tau_{ik} - u_k p - q_k]. \quad (3)$$

The fluid density is denoted by  $\rho$ , time by  $t$ , fluid velocity by  $u_i$ . The total energy  $E$  can be computed from

$$E = \frac{T}{[\gamma(\gamma-1)M^2]} + \frac{1}{2}u_i u_i, \quad (4)$$

where  $T$  is the temperature. The stress tensor  $\tau_{ik}$  and heat-flux  $q_k$  are given as

$$\tau_{ik} = \frac{\mu}{Re} \left( \frac{\partial u_i}{\partial x_k} + \frac{\partial u_k}{\partial x_i} - \frac{2}{3} \frac{\partial u_k}{\partial x_k} \delta_{ik} \right), \quad (5)$$

$$q_k = \frac{-\mu}{(\gamma-1)M^2 Pr Re} \frac{\partial T}{\partial x_k}. \quad (6)$$

The Reynolds number is set to 1000 and is defined in terms of the freestream velocity  $U_0$  and the plate chord length  $L_0$  as  $Re = \rho U_0 L_0 / \mu$ . Two different freestream Mach numbers are considered at  $M = U_0 / c = 0.4$  and  $0.6$ , where  $c$  is the speed of sound. The Prandtl number and the ratio of the specific heat are taken to be constant at  $Pr = 0.72$  and  $\gamma = 1.4$ . Sutherland's law [22] is used to compute the molecular viscosity  $\mu$  with the Sutherland constant of 0.3686. The system of equations is closed by solving the non-dimensional equation of state to obtain the pressure  $p$  as

$$p = \frac{\rho T}{\gamma M^2}. \quad (7)$$

The computations are performed via an in-house compressible DNS code, HiPSTAR. The code uses a standard 4<sup>th</sup>-order central finite-difference scheme with a boundary treatment of Carpenter *et al.* [23] to discretise the spatial derivatives in the streamwise ( $x$ ) and transverse ( $y$ ) directions. An ultra-low-storage five-step 4<sup>th</sup>-order Runge–Kutta scheme [24] is employed for the temporal integration. A skew-symmetric splitting scheme of the convective terms and the 12-point explicit filtering of Bogey *et al.* [25] are used to enhance the stability of the flow solver. The code has been validated with various benchmark cases and has been used to investigate several flow problems (see, e.g., Sandberg [14]). To represent the inclined flat plate, a second-order boundary data immersion method (BDIM) [26] for compressible flow is employed. The capability of the compressible BDIM to represent noise generation from stationary and moving bodies is also demonstrated in Schlanderer *et al.* [26].

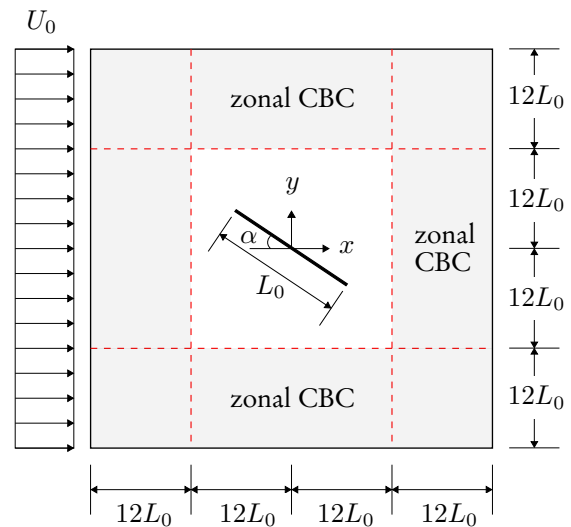


Fig. 1. Schematic of the computational domain of flow over an inclined plate.

The sketch of the computational domain for the inclined-plate flow is shown in Fig. 1. The computational domain is chosen in such a way that the grid resolution is well resolved up to the distance of the acoustic wavelength,  $\lambda_a = c/f$ , for the frequency  $f/f_{in} = 0.43$ , where  $f_{in}$  is the most dominant frequency of the spectrum of the far-field. This results in the measurement region of  $-12 \leq (x, y)/L_0 \leq 12$ . The domain length in both directions is then extended twice to allow acoustic waves and wake vortices to exit the domain without spurious reflections.

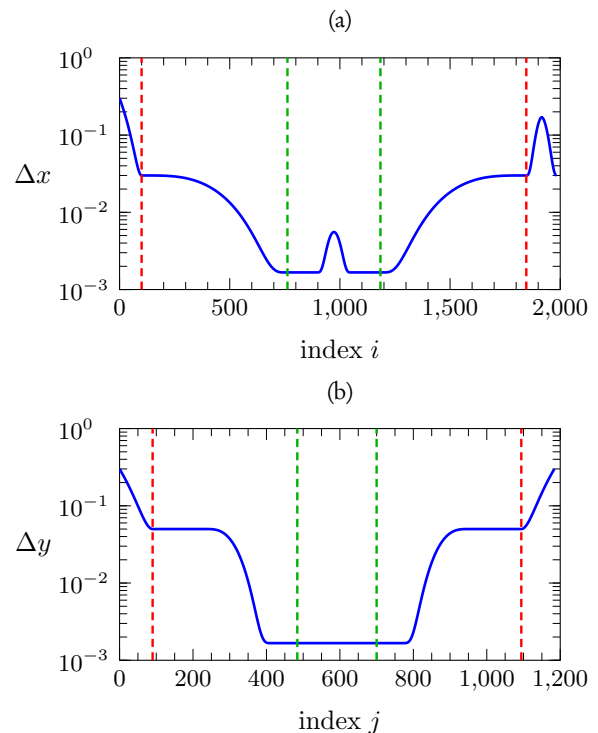


Fig. 2. Distribution of grid spacing in (a) streamwise  $\Delta x$  and (b) transverse  $\Delta y$  directions. Red dashed lines indicate the measurement region, while green dashed lines show the plate location.

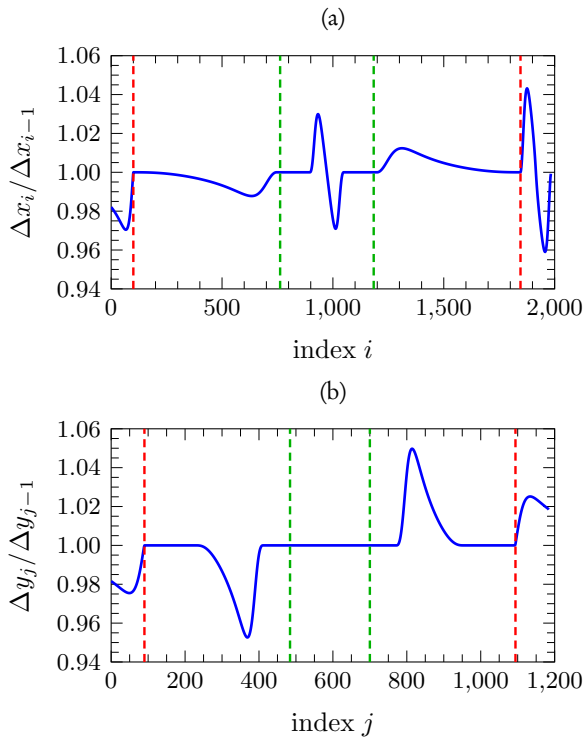


Fig. 3. Distribution of grid stretching in (a) streamwise and (b) transverse directions. Red dashed lines indicate the measurement region, while the green dashed lines show the plate location.

In this work, the acoustic waves in the far-field measurement region are resolved with about ten grid points per acoustic wavelength up to a frequency of  $f_{\text{res}} = 10f_{\text{in}}$ . This means that the grid resolution in the mean-flow normal direction is  $\Delta y = c/f_{\text{res}}/10 = 0.05L_0$  (Fig. 2). Since the propagation speed of the acoustic wave in a negative  $x$ -direction reduces to  $c = U_0/M - U_0$ , the resolution in the  $x$ -direction is set to  $\Delta x = 0.03L_0$ . The thickness of the sharp leading edge and trailing edge is discretised with more than 10 grid points to capture the strongest gradients that are expected to occur due to the geometric singularity. Additionally, the grid aspect ratio at these locations is set to be unity. At the inflow, top and bottom of the domain, the grid spacing at these locations is quite coarse ( $\Delta x = \Delta y = 0.03L_0$ ) in order to damp the acoustic waves propagating out of the computational domain. In contrast, the resolution at the outflow zone is decreased but then increased to ensure that both the acoustic waves

and the vortical structures leave the domain smoothly. The grids in each zone are linked together by a high-order polynomial function, resulting in the total grid points used of  $1984 \times 1185$ . The grid stretching in both directions is kept lower than 5% in order to avoid any spurious effect (Fig. 3). For the calculations of both Mach numbers, a nondimensional timestep is fixed at  $\Delta t = 2.5 \times 10^{-3}$ . This yields the maximum Courant–Friedrichs–Lewy (CFL) number of about 1.0, which ensures the requirements of the numerical stability.

At the inflow, a uniform velocity is prescribed using an integrated characteristic boundary condition (iCBC). A zonal CBC [27] is employed to avoid any spurious waves at the outflow (for  $x/L_0 \geq 12$  with 137 points) and at the freestream boundaries with 90 points in each direction. In this work, the angle of attack of the plate is  $\alpha = 20^\circ$ . The plate thickness is set to  $0.02L_0$  with sharp leading edge and trailing edge.

### 3. Results

In this section, we present numerical results of flow over an inclined plate at incidence of  $20^\circ$  and Mach numbers of 0.4 and 0.6. A check of the grid convergence is first performed in Sec. 3.1. The effect of the Mach number on the hydrodynamic field is examined in Sec. 3.2. Finally, the acoustic noise generated by an inclined plate is investigated in Sec. 3.3.

#### 3.1. Grid Convergence Test

As the number of grid points used can alter the accuracy of the numerical results and the computational times, it is necessary to perform a grid convergence test to find the optimal grid resolution for this work. The grid convergence test has been performed at 3 levels of grid resolution by varying the number of grid points only in the region of the leading edge and the trailing edge, while the resolution of the far field remains unchanged. Table 1 summarises the number of grid points used and the minimum grid spacing occurring at the leading edge and the trailing edge for three different resolution levels. The numerical values of the time-averaged lift coefficients  $\overline{C}_L = \overline{F}_L/0.5\rho_0U_0^2L_0$ , time-averaged drag coefficient  $\overline{C}_D = \overline{F}_D/0.5\rho_0U_0^2L_0$ , and

Grid fineness	$N_x \times N_y$	$(\Delta x_{\text{min}}, \Delta y_{\text{min}})$	$\overline{C}_D$	$\overline{C}_L$	$St$
Coarse grid	$1840 \times 1041$	$2.5 \times 10^{-3}$	0.4979	1.0725	0.4879
Medium grid	$1984 \times 1185$	$1.67 \times 10^{-3}$	0.4966	1.0719	0.4879
Fine grid	$2192 \times 1401$	$1.11 \times 10^{-3}$	0.4960	1.0720	0.4879

Table 1. Number of grid points and minimum spacing together with its effect on dimensionless quantities at  $Re = 1000$  and  $M = 0.4$ .

the Strouhal number  $St = fL_0/U_0$  obtained from the three cases are also given in Table 1. It can be seen that  $\overline{C}_L$  and  $\overline{C}_D$  are slightly different between the intermediate and the fine grids, while  $St$  of all grid levels is exactly the same. Therefore, the medium grid level is used throughout this work to reduce the computational cost.

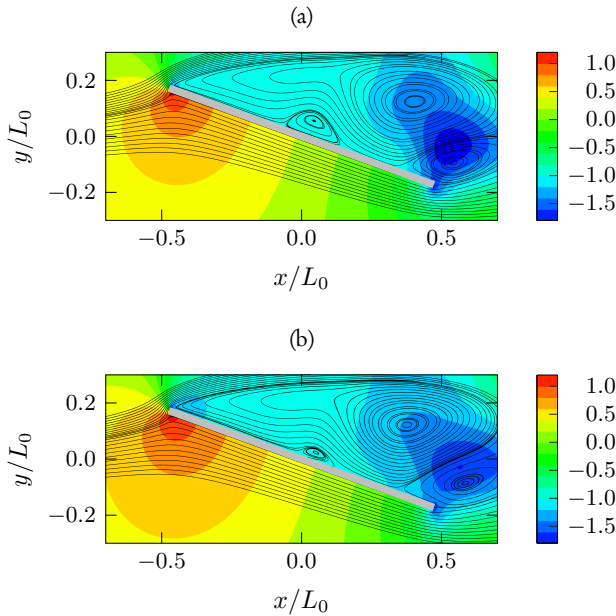


Fig. 4. Time-averaged streamlines together with contours of time-averaged pressure coefficient of flow over an inclined plate at (a)  $M = 0.4$  and (b)  $M = 0.6$ .

### 3.2. Hydrodynamic Field

This section examines the effects of the Mach numbers on the near-field behaviour of flow past an inclined plate at incidence of  $20^\circ$ . The focus is on its effects on the aerodynamic characteristics and the formation of the vortex shedding. The time-averaged flow fields near the plate are investigated by means of the streamlines and the contours of the time-averaged pressure coefficient  $\overline{C}_p = (\overline{p} - p_0)/0.5\rho U_0^2$ , as shown in Fig. 4. As expected, recirculation regions due to the flow separation occur on the suction side around the middle of the plate and near the trailing edge. The first recirculation region is usually referred to as a *laminar separation bubble*. If a three-dimensional simulation at relatively high Reynolds number were conducted, the flow would undergo rapid transition to turbulence after the reattachment of the separated shear layer. It can be seen that the formation of the separation bubble is clearly influenced by the Mach number. As illustrated in Fig. 4(b), the size of the separation bubble looks smaller when the Mach number increases (supported by the evidence in Figure 6 below). In contrast, the shape of the leading-edge and trailing-edge vortices of both cases is almost identical.

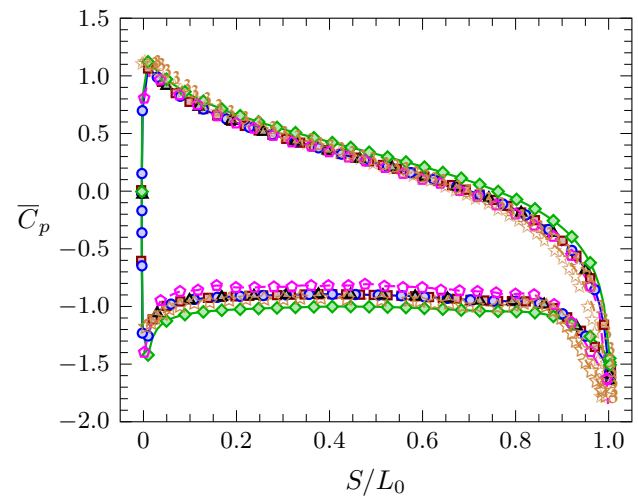


Fig. 5. Distribution of time-averaged pressure coefficient  $\overline{C}_p$  along the pressure and suction sides:

■  $M = 0.4$  (coarse grid); ●  $M = 0.4$  (medium grid); ▲  $M = 0.4$  (fine grid); ◆  $M = 0.6$ ; ☆ Yang *et al.* [17]; ☆ Li *et al.* [28].

Figure 5 displays the distribution of  $\overline{C}_p$  on both sides of the plate along the distance of the plate surface  $S$ . The pressure maximum occurs on the plate lower side near the leading edge. The pressure then decreases monotonically towards the lee side. The trailing-edge vortex on the suction side results in the presence of the pressure minimum, while the pressure distribution in a separation bubble region is nearly constant. The profile of  $\overline{C}_p$  is also compared with the published results from incompressible flow simulations [17, 28]. It can be seen that the present data at  $M = 0.4$  match well with the previous incompressible works although slight discrepancies occur on the suction side especially near the trailing edge, due to different formation of the separation bubble. Moreover,  $\overline{C}_p$  from three different resolutions collapses on to one curve. This also confirms that the grid resolution used is sufficiently fine to capture the surface pressure. For higher Mach number  $M = 0.6$ , the magnitude of  $\overline{C}_p$  on both sides of the plate is slightly larger, although the distribution of  $\overline{C}_p$  seems to be almost the same to that of the lower Mach number ( $M = 0.4$ ).

The profile of the time-averaged skin-friction coefficient,  $\overline{C}_f = 2\overline{\tau}_w/\rho U_0^2$  (where  $\overline{\tau}_w$  being the time-averaged wall shear stress), is shown in Fig. 6. The flow separation can be determined from the zero-crossing of the  $\overline{C}_f$ . It can be seen that flow on the pressure side is attached to the plate due to a favourable pressure gradient. In contrast, a region of flow separation is observed on the suction side. For  $M = 0.4$ , the onset of the separation bubble occurs at  $S/L_0 \approx 0.44$  with the bubble length of about 0.21. As the Mach number increases to 0.6, the bubble length decreases to 0.12, while its onset is shifted to  $S/L_0 \approx 0.50$ . This also confirms the

effect of the Mach number on the formation of the separation bubble illustrated in Fig. 4. It is worth noting that the profile of  $\bar{C}_f$  of the fine grid and medium grid cases seems to collapse onto one curve, while that of the coarse grid is slightly underpredicted, especially near the trailing edge ( $S/L_0 > 0.85$ ). This verifies that the grid resolution used is sufficient to fully resolve the laminar separation bubble.

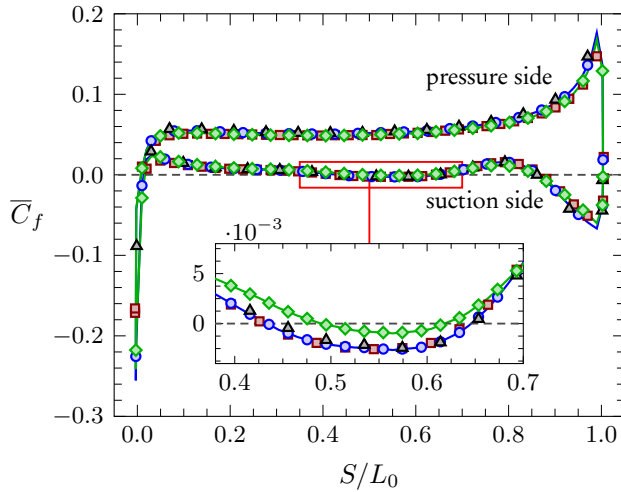


Fig. 6. Profile of time-averaged skin-friction coefficient  $\bar{C}_f$  along the pressure and suction sides of the flat plate:  $\square$   $M = 0.4$  (coarse grid);  $\circ$   $M = 0.4$  (medium grid);  $\triangle$   $M = 0.4$  (fine grid);  $\diamond$   $M = 0.6$ .

	$M$	$\bar{C}_D$	$\bar{C}_L$	$St$
Yang <i>et al.</i> [17]	0.0	...	1.0381	0.4881
Li <i>et al.</i> [28]	0.0	0.4463	1.0560	0.4876
Present DNS	0.4	0.4966	1.0719	0.4879
	0.6	0.5544	1.2389	0.5270

Table 2. Comparison of dimensionless quantities of flow over an inclined plate at  $\alpha = 20^\circ$  and  $Re = 1000$ . Note that  $M = 0.0$  represents incompressible flow simulation.

The numerical values of the dimensionless quantities, i.e. the time-averaged drag  $\bar{C}_D$  and lift  $\bar{C}_L$  coefficients and the Strouhal number  $St$ , are given in Table 2. The magnitude of  $\bar{C}_D$  and  $\bar{C}_L$  increases with the Mach number due to the higher pressure (supported by the evidence provided in Fig. 9b). The vortex shedding frequency for  $M = 0.6$  is also found to slightly increase. When comparing the present data with the incompressible results of Yang *et al.* [17] and Li *et al.* [28], reasonable agreement is obtained with a slight over-prediction because of the Mach number difference.

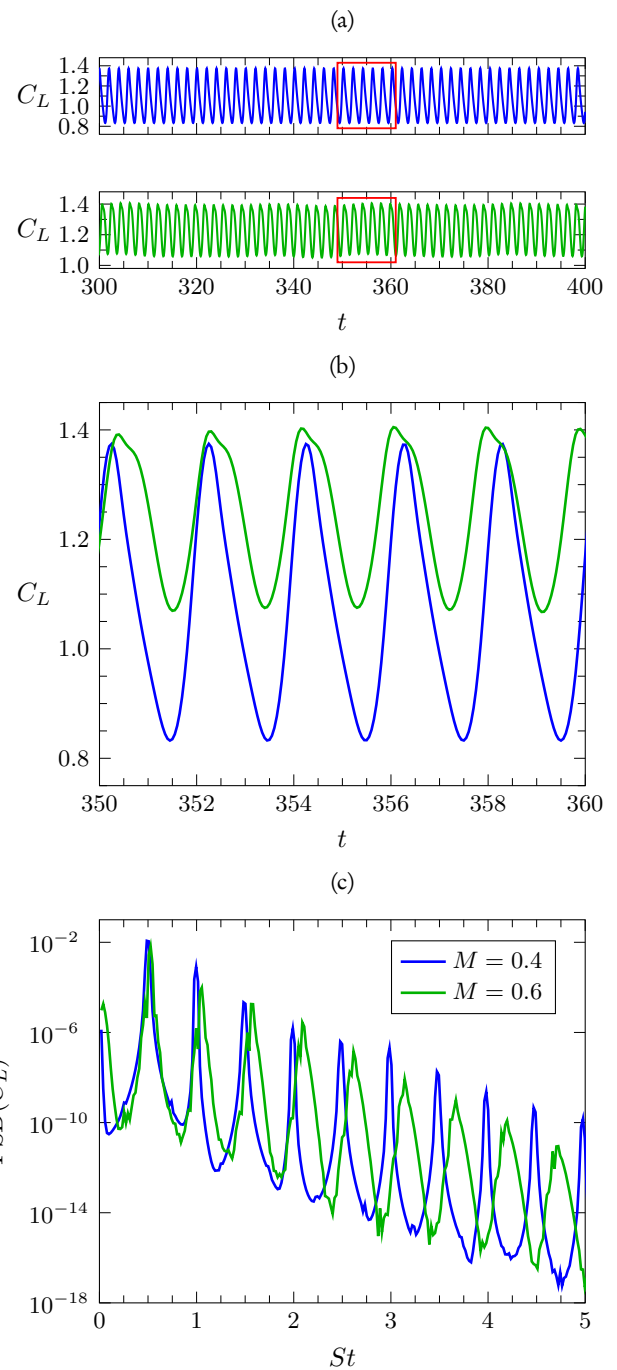


Fig. 7. (a) Histories of the lift coefficient  $C_L$  together with (b) the enlarged view. (c) Power spectral density (PSD) of the lift coefficient.

Histories of the lift coefficient for the shedding period of about 50 are illustrated in Fig. 7(a), with an enlarged view at  $350 \leq t \leq 360$  (Fig. 7b). It can be seen that  $C_L$  for both cases exhibits a periodic signal. The lift coefficient of  $M = 0.4$  has higher fluctuating magnitude than that of  $M = 0.6$ . The power spectral density (PSD) of the lift coefficient is shown in Fig. 7(c). The most dominant non-dimensional shedding frequency, the Strouhal number  $St$ , for  $M = 0.4$  is  $St = 0.4879$ . The second and higher harmonics of the shedding frequency are clearly observed. As the Mach number increases, it is found that  $St$  slightly increases to 0.5270.

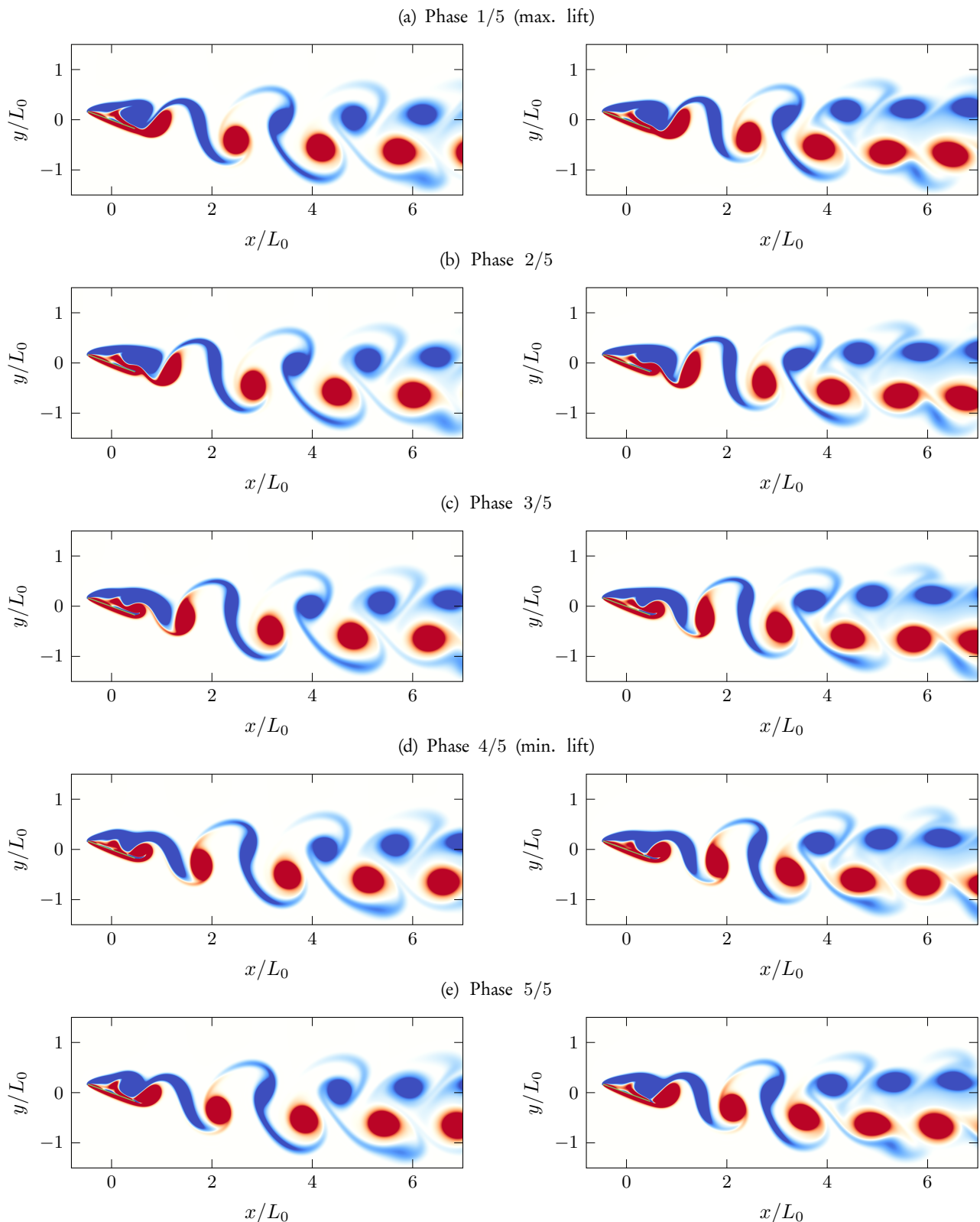


Fig. 8. Contours of instantaneous vorticity  $\omega$  at consecutive phases in one shedding cycle of flow over an inclined plate at (left column)  $M = 0.4$  and (right column)  $M = 0.6$ . Vorticity varies from  $-2 < \omega < 2$ . Blue and red patches respectively show negative and positive vorticity.

The instantaneous vorticity at consecutive phases during one shedding cycle is visualised to investigate the pattern of the flow fields around the flat plate at two different Mach numbers, as shown in Fig. 8. For both Mach numbers, the vortices are shed periodically from

the plate. The vortex shedding consists of the positive counterclockwise-rotating vortex, that forms due to the roll-up of the shear layer at the trailing edge, followed by the negative clockwise-rotating vortex generated from the leading edge. The maximum lift occurs when the

TEV is pushed away from the plate by the fully formed LEV, as shown in Fig. 8(a). At that time, the LEV moves closest to the upper plate surface. This yields the largest region of the suction pressure, resulting in the highest normal force. After that instance, the LEV is pushed far away from the plate by a newly formed TEV (Figs. 8b – 8c). This results in lower suction pressure leading to a decrease in the lift. Once the LEV is moved farthest, the plate experiences the minimum lift (Fig. 8d). The TEV is then grow to maturity, while the LEV becomes bigger and move close to the plate upper surface again, which yields an increase in the lift (Fig. 8e). As the shedding frequency increases with the Mach number, the space between each vortex pair of  $M = 0.6$  becomes closer. This results in an increase in the number of the mushroom-like vortex pairs in the wake region.

### 3.3. Acoustic Field

As this work aims to investigate the acoustic noise generated by an inclined plate, it is essential to ensure that the acoustic field is represented accurately. Figure 9 illustrates the history of the pressure normalised by the freestream pressure  $p/p_\infty$  in the far-field region at the radial distance of  $r/L_0 = 11.9$  and  $\theta = 270^\circ$  ( $x/L_0 = 0$  and  $y/L_0 = -11.9$ ), together with its power spectral density (PSD). The far-field pressure of both cases exhibits a sinusoidal shape, but with different amplitudes and patterns, as displayed in Fig. 9(a). For  $M = 0.6$ , the amplitude of the far-field pressure is slightly higher. Additionally, the signal of  $p/p_\infty$  for this Mach number is more unstable. Figure 9(b) reveals that the most dominant frequency of the acoustic far-field for both cases is equal to the vortex shedding frequency. This results in a decrease in the acoustic wavelength of  $\lambda_a = c/f = 5.12$  for  $M = 0.4$  to  $\lambda_a = 3.16$  for  $M = 0.6$  (see Fig. 11 below).

The decay of the acoustic pressure, represented by the plot of the root-mean-square pressure  $p_{\text{rms}}$  along the negative transverse direction starting from the trailing-edge, is displayed in Fig. 10. The distribution of the  $p_{\text{rms}}$  for both Mach numbers is almost identical. It is observed that the  $p_{\text{rms}}$  in the near and far fields decays with different scaling laws. The acoustic pressure fluctuations in the near field can be approximated as  $p_{\text{rms}} \sim 1/r$ . However, for larger values of  $r$ , the acoustic pressure decreases with a slower rate as  $p_{\text{rms}} \sim 1/\sqrt{r}$ .

Figure 11 displays the contour plots of the dilatation field,  $\nabla \cdot \mathbf{u}$ , at an arbitrary instance of time in order to visualise the resulting acoustic field. For both Mach numbers, it can be clearly seen that acoustic waves originate from the trailing edge of the plate. The strongest scattering is observed in the southwest direction with an increase in an acoustic noise level on the plate suction side

due to the interaction between the surface pressure fluctuations due to the flow separation and the associated vortex shedding. The acoustic noise level seems to increase with an increase in the Mach number. Moreover, it is clearly seen that the acoustic wavelength decreases as the Mach number increases. It should be noted that there are no signs of spurious pressure reflections from any boundaries of the computational domain into the region of interest. This confirms the choice of the domain length and the boundary conditions used.

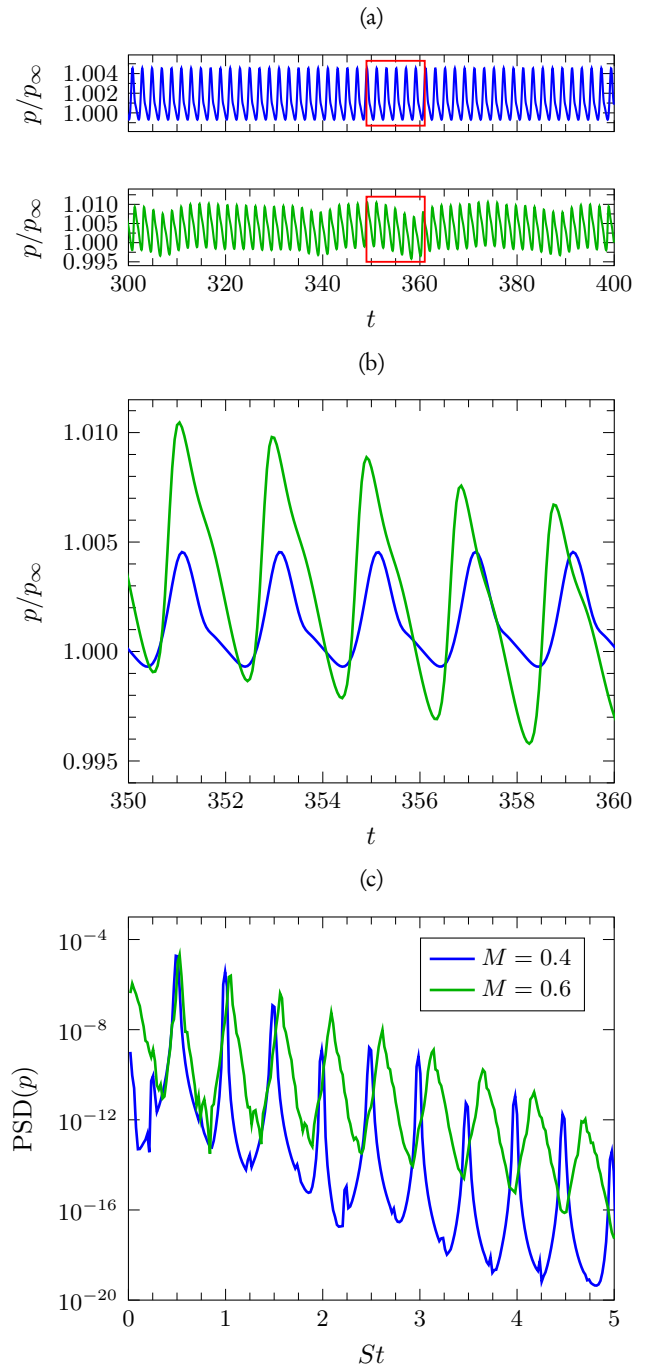


Fig. 9. (a) Histories of the nondimensional pressure  $p/p_\infty$  at  $\theta = 270^\circ$  and  $r/L_0 = 11.9$  together with (b) the enlarged view. (c) Power spectral density (PSD) of the pressure.

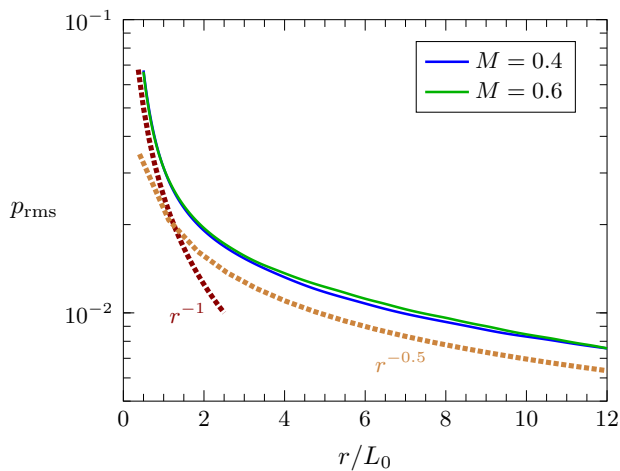


Fig. 10. Root-mean-square acoustic pressure radiated from the trailing-edge along the negative transverse direction.

The distribution of the acoustic pressure fluctuations radiated from the trailing edge along the azimuthal direction at the radial distance of  $r/L_0 = 10$  is plotted in Fig. 12. The directivity of the sound pressure level,  $SPL = 20 \log_{10}(p_{rms}/p_{\infty})$ , for both cases is quite different, especially in the upper half of the computational domain. For  $M = 0.4$ , the pressure fluctuation exhibits one lobe on the suction side and one bigger lobe on the pressure side with the maximum SPL at  $\theta \approx 250^\circ$  (Fig. 12a). Note that the results from the coarse grid and fine grid resolutions are also plotted in Fig. 12(a) to show that all three grid resolution levels yield the same shape of the directivity pattern. Although the pressure fluctuation of  $M = 0.6$  shows one big lobe on the pressure side similar to the lower Mach number case, its direction points slightly closer to the trailing edge (Fig. 12b). The major effect of increasing Mach number can be seen on the suction side, in which three lobes are observed with bigger SPL. Note that the observation of additional lobes at higher Mach number was also found in the computation of the trailing-edge noise [8]. The minimum pressure fluctuation is found to occur at  $\theta \approx 135^\circ$ , as also illustrated in the dilatation contour plot in Fig. 11(b).

#### 4. Conclusions

Two-dimensional numerical simulations of unsteady compressible flow around an inclined flat plate are performed at two different Mach numbers without any aeroacoustic source models. The numerical results show that increasing Mach number can remarkably influence the directivity of the acoustic noise radiated from the plate and the formation of the vortex shedding. The vortex shedding frequency slightly increases from  $St = 0.4879$  to  $0.5270$  with an increase

in the Mach number. Increasing the Mach number increases the values of the time-averaged drag and time-averaged lift coefficients. The numerical value of  $\bar{C}_D$  changes from 0.4966 to 0.5544, while that of  $\bar{C}_L$  rises from 1.0719 to 1.2389. The Mach number also alters the distribution of the skin-friction coefficient, leading to the modification of the resulting separation bubble. The size of the bubble for the higher Mach number case is found to be smaller. The computed acoustic field shows that the acoustic wavelength decreases with an increase in the Mach number. Furthermore, the directivity of the acoustic pressure fluctuation on the suction side exhibits additional lobes at higher Mach number.

#### Acknowledgement

The authors acknowledge the support of the Thailand Science Research and Innovation (TSRI) under Grant No. MRG6280157, with Prof. Dr. Vejapong Juttijudata as the program mentor. NB would like to acknowledge the support from the Faculty of Engineering (Research Assistant Program) and the Graduate School CMU (Teaching Assistant and Research Assistant). The computational resources provided by the National e-Science Infrastructure Consortium are highly appreciated.

#### References

- [1] T. F. Brooks, D. S. Pope, and M. A. Marcolini, "Airfoil self-noise and prediction," NASA, Tech. Rep. NASA Reference Publication 1218, 1989.
- [2] J. E. Ffowcs Williams and L. H. Hall, "Aerodynamic sound generation by turbulent flow in the vicinity of a scattering half plane," *J. Fluid Mech.*, vol. 40, no. 4, pp. 657–670, 1970.
- [3] M. J. Lighthill, "On sound generated aerodynamically I. General theory," *Proc. R. Soc. London Ser. A-Math. Phys. Sci.*, vol. 211, no. 1107, pp. 564–587, 1952.
- [4] M. J. Lighthill, "On sound generated aerodynamically II. Turbulence as a source of sound," *Proc. R. Soc. London Ser. A-Math. Phys. Sci.*, vol. 222, no. 1148, pp. 1–32, 1954.
- [5] M. S. Howe, "A review of the theory of trailing edge noise," *J. Sound Vibr.*, vol. 61, no. 3, pp. 437–465, 1978.
- [6] R. K. Amiet, "Noise due to turbulent flow past a trailing edge," *J. Sound Vibr.*, vol. 47, no. 3, pp. 387–393, 1976.
- [7] T. F. Brooks and T. H. Hodgson, "Trailing edge noise prediction from measured surface pressures," *J. Sound Vibr.*, vol. 78, no. 1, pp. 69–117, 1981.

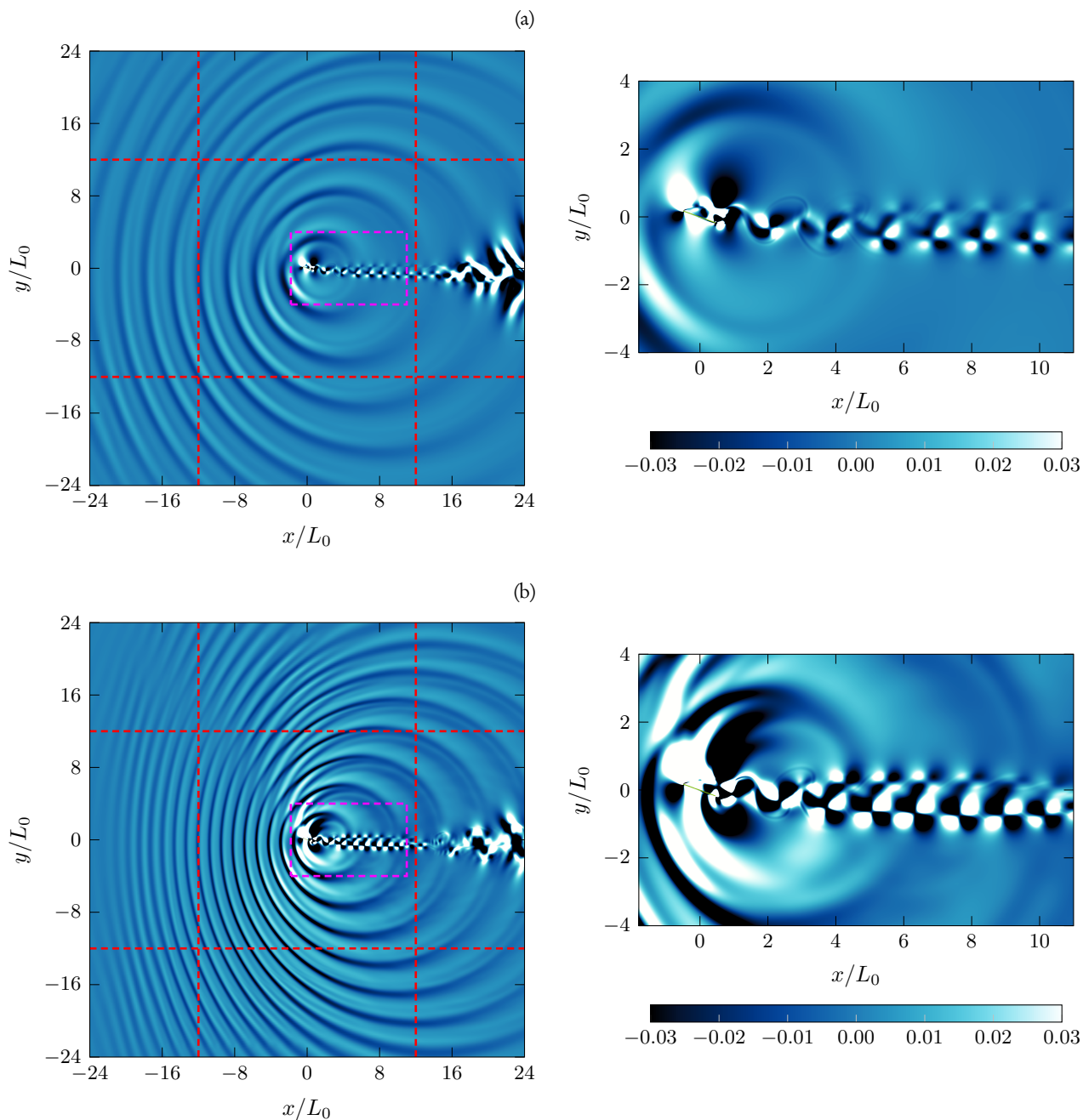


Fig. 11. Instantaneous contours of dilatation  $\nabla \cdot \mathbf{u}$  of flow over an inclined plate at (a)  $M = 0.4$  and (b)  $M = 0.6$ . The enlarged figures around the plate shown in the pink dashed box are given in the right column. The red dashed lines indicate the beginning of the zonal CBC.

- [8] R. D. Sandberg, N. D. Sandham, and P. F. Joseph, "Direct numerical simulations of trailing-edge noise generated by boundary-layer instabilities," *J. Sound Vibr.*, vol. 304, no. 3–5, pp. 677–690, 2007.
- [9] R. W. Paterson, P. G. Vogt, M. R. Fink, and C. L. Munch, "Vortex noise of isolated airfoils," *J. Aircr.*, vol. 10, no. 5, pp. 296–302, 1973.
- [10] R. H. Schlinker, M. R. Fink, and R. K. Amiet, "Vortex noise from nonrotating cylinders and airfoils," in *14th Aerospace Sciences Meeting*, Washington, DC, USA, 26–28 January 1976.
- [11] B. A. Singer, K. S. Brentner, D. P. Lockard, and G. M. Lilley, "Simulation of acoustic scattering from a trailing edge," *J. Sound Vibr.*, vol. 230, no. 3, pp. 541–560, 2000.
- [12] G. Desquesnes, M. Terracol, and P. Sagaut, "Numerical investigation of the tone noise mechanism over laminar airfoils," *J. Fluid Mech.*, vol. 591, pp. 155–182, 2007.
- [13] R. D. Sandberg, L. E. Jones, N. D. Sandham, and P. F. Joseph, "Direct numerical simulations of tonal noise generated by laminar flow past airfoils," *J. Sound Vibr.*, vol. 320, no. 4–5, pp. 838–858, 2009.

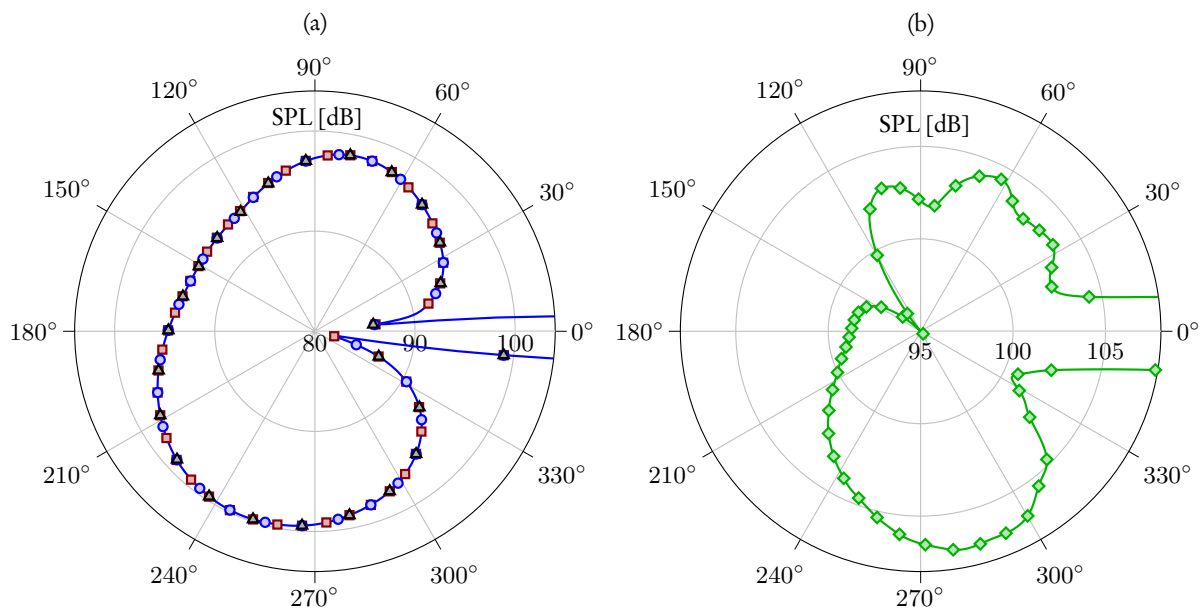


Fig. 12. Directivity of the acoustic pressure fluctuation radiated from the trailing edge at a radial distance of  $r/L_0 = 10$ . (a)  $M = 0.4$  (■ coarse grid; ● medium grid; ▲ fine grid) and (b)  $M = 0.6$ .

- [14] R. D. Sandberg, "Compressible-flow DNS with application to airfoil noise," *Flow Turbul. Combust.*, vol. 95, no. 2–3, pp. 211–229, 2015.
- [15] A. Eltaweel and M. Wang, "Numerical simulation of broadband noise from airfoil-wake interaction," in *17th AIAA/CEAS Aeroacoustics Conference (32nd AIAA Aeroacoustics Conference)*, Portland, OR, USA, 5–8 June 2011.
- [16] E. Manoha, C. Herrero, P. Sagaut, and S. Reonnet, "Numerical prediction of airfoil aerodynamic noise," in *8th AIAA/CEAS Aeroacoustics Conference & Exhibit*, Breckenridge, CO, USA, 17–19 June 2002.
- [17] D. Yang, B. Pettersen, H. I. Andersson, and V. D. Narasimhamurthy, "Vortex shedding in flow past an inclined flat plate at high incidence," *Phys. Fluids*, vol. 24, no. 8, p. 084103, 2012.
- [18] D. Yang, B. Pettersen, H. I. Andersson, and V. D. Narasimhamurthy, "Floquet stability analysis of the wake of an inclined flat plate," *Phys. Fluids*, vol. 25, no. 9, p. 094103, 2013.
- [19] K. M. Lam and C. T. Wei, "Numerical simulation of vortex shedding from an inclined flat plate," *Eng. Appl. Comp. Fluid Mech.*, vol. 4, no. 4, pp. 569–579, 2010.
- [20] K. M. Lam and M. Y. H. Leung, "Asymmetric vortex shedding flow past an inclined flat plate at high incidence," *Eur. J. Mech. B-Fluids*, vol. 24, no. 1, pp. 33–48, 2005.
- [21] M. Breuer and N. Jovičić, "Separated flow around a flat plate at high incidence: An LES investigation," *J. Turbul.*, vol. 2, no. N18, pp. 1–15, 2001.
- [22] F. M. White, *Viscous Fluid Flow*, 3rd ed. New York, NY: McGraw-Hill, 2006.
- [23] M. H. Carpenter, J. Nordström, and D. Gottlieb, "A stable and conservative interface treatment of arbitrary spatial accuracy," *J. Comput. Phys.*, vol. 148, no. 2, pp. 341–365, 1999.
- [24] C. A. Kennedy, M. H. Carpenter, and R. M. Lewis, "Low-storage, explicit Runge–Kutta schemes for the compressible Navier–Stokes equations," *Appl. Numer. Math.*, vol. 35, no. 3, pp. 177–219, 2000.
- [25] C. Bogey, N. de Cacqueray, and C. Bailly, "A shock-capturing methodology based on adaptive spatial filtering for high-order non-linear computations," *J. Comput. Phys.*, vol. 228, no. 5, pp. 1447–1465, 2009.
- [26] S. C. Schlanderer, G. D. Weymouth, and R. D. Sandberg, "The boundary data immersion method for compressible flows with application to aeroacoustics," *J. Comput. Phys.*, vol. 333, p. 440–461, 2017.
- [27] R. D. Sandberg and N. D. Sandham, "Nonreflecting zonal characteristic boundary condition for direct numerical simulation of aerodynamic sound," *AIAA J.*, vol. 44, no. 2, p. 402–405, 2006.
- [28] Z. Li, C. Lan, L. Jia, and Y. Ma, "Ground effects on separated laminar flows past an inclined flat plate," *Theor. Comput. Fluid Dyn.*, vol. 31, no. 2, pp. 127–136, 2017.

**Nonwarit Borvornsareepirom**, photograph and biography not available at the time of publication.

**Watchapon Rojanaratanangkule**, photograph and biography not available at the time of publication.